PAMM

SPECIAL ISSUE 95th Annual Meeting of the International Association of Applied Mathematics and Mechanics (GAMM)

RESEARCH ARTICLE OPEN ACCESS

Multiphase-Field Modeling of Discontinuous Dynamic Recrystallization

H.A.T. Vimukthi Nanayakkara[1] | Rupesh Chafle[1] | Benjamin Klusemann[1,2]

[1]Helmholtz-Zentrum Hereon, Institute of Material and Process Design, Solid State Materials Processing, Geesthacht, Germany | [2]Leuphana University Lüneburg, Institute for Production Technology and Systems, Lüneburg, Germany

Correspondence: H.A.T. Vimukthi Nanayakkara (halloluwa.nanayakkara@hereon.de)

Received: 26 June 2025 | **Revised:** 9 December 2025 | **Accepted:** 31 December 2025

ABSTRACT

Solid-state processing techniques such as friction extrusion and friction surfacing have emerged as advanced methods for processing metallic alloys. These techniques utilize frictional heat and severe mechanical deformation to drive microstructure changes without reaching the melting point. However, the severe thermo-mechanical conditions during such processes make experimental characterization of microstructure evolution challenging. To address this, numerical modeling becomes essential for predicting microstructure behavior and guiding process optimization. This study presents a computational framework based on the multiphase-field (MPF) method to investigate the discontinuous dynamic recrystallization (DDRX) mechanism occurring during these processes. The MPF method is utilized to model grain nucleation and boundary migration, incorporating the effects of dislocation dynamics through the implementation of the Kocks–Mecking model. This framework establishes a direct correlation between microstructure evolution and the macroscopic mechanical behavior observed during DDRX.

1 | Introduction

Al alloys are widely utilized in contemporary engineering applications due to their excellent strength-to-weight ratio, remarkable resistance to corrosion, and high recyclability attributes that are particularly beneficial in the automotive and aerospace sectors [1]. These advantageous properties stem from the complex interrelationship among the alloy's chemical composition, microstructure characteristics, and thermo-mechanical processing history. Notably, the formation and transformation of various precipitate phases, along with the development of a recrystallized microstructure, play a crucial role in determining their mechanical performance [2, 3]. Solid-state processing methods enable the deformation of materials at temperatures below their melting point through plastic deformation. For this project, in particular, friction extrusion (FE) and friction surfacing (FS) are considered relevant to examine the microstructure evolution [3, 4].

The dominant microstructure transformation occurring during FE and FS is dynamic recrystallization (DRX), which facilitates the formation of new, strain-free grains by reducing dislocation density during plastic deformation [5, 6]. Recrystallization during deformation can manifest in three distinct forms: discontinuous dynamic recrystallization (DDRX), continuous dynamic recrystallization (CDRX), and geometric dynamic recrystallization (GDRX) [7]. DDRX generally occurs in metals possessing low to medium stacking fault energy, while CDRX is more prevalent in materials with high stacking fault energy, such as Al alloys. However, it has been shown that friction-based processing leads to a complex interplay between CDRX and DDRX in Al alloys [3, 4]. The experimental investigation on FS of dissimilar Al alloys [3] reported the simultaneous occurrence of CDRX and DDRX, where recrystallized grains are observed along high-angle grain boundaries, often forming structures resembling necklace as a result of the deformation process.

Solid-state processing is characterized by severe plastic deformation, which poses significant challenges for the direct experimental observation of microstructure evolution. Consequently, numerical modeling serves as an essential approach for investigating microstructure evolution during severe plastic deformations. Several numerical modeling strategies have been developed to investigate microstructure evolution during DDRX, including Cellular Automata (CA) [8], Monte Carlo (MC) [9], and Phase-field (PF) methods. Despite their utility, both CA and MC models exhibit inherent limitations, such as difficulties in accurately capturing temporal evolution and grain boundary migration governed by curvature effects [10, 11]. In contrast, the PF approach, which utilizes diffuse interfaces, provides significant flexibility in representing complex microstructure features. This method eliminates the need for explicit interface tracking, thereby enabling more robust and realistic simulations of grain structure evolution under dynamic processing conditions [12]. For capturing DDRX–CDRX interaction, Takaki and Tomita [13] proposed coupling dislocation-density-based stored energy to the driving force for grain-boundary migration (i.e., DDRX) and linking stored energy, grain-boundary mobility, and grain-boundary energy to misorientation evolution to model subgrain formation and the progressive transition from low-angle to high-angle boundaries (i.e., CDRX).

As a first step in modeling the complex microstructure evolution in solid-state materials processing, an MPF modeling framework is employed to simulate microstructure evolution during DDRX. The MPF model used in this study was originally developed by Steinbach and Pezzolla [14], and later employed by Takaki et al. [10] to simulate DDRX. In the present work, we implement the model proposed by Takaki et al. [10] using a finite difference method to investigate DDRX phenomena under different strain rates.

2 | Numerical Model

2.1 | Multiphase-Field Model

In the present multiphase-field (MPF) model, each grain i is characterized by a corresponding phase-field variable ϕ_i, such that $\phi_i = 1$ denotes the full presence of phase i, while $\phi_i = 0$ signifies its complete absence. At interfaces, ϕ_i smoothly transitions between 0 and 1. To ensure conservation of the total phase fraction at every spatial location, the sum of the local phase fields ϕ_i can be expressed as [15]

$$\sum_{i=1}^{N} \phi_i(x) = 1, \tag{1}$$

where N denotes the total number of local phase fields. The total free energy functional Ψ is defined as the volume integral over the entire volume Ω, accounting for both the interfacial free energy density ψ^{int} and the bulk free energy density ψ^{b}, and is determined by

$$\Psi = \int_{\Omega} \left[\psi^{int} + \psi^{b}\right] d\Omega. \tag{2}$$

The ψ^{int} is given by

$$\psi^{int} = \sum_{i=1}^{N} \sum_{j \neq i}^{N} \left[W_{ij}\phi_i\phi_j - \frac{a_{ij}^2}{2} \nabla\phi_i \cdot \nabla\phi_j \right], \tag{3}$$

where a_{ij} denotes the gradient energy coefficient between phases i and j, while W_{ij} is the height of the energy barrier. By introducing the pairwise interaction function, the evolution equation for the phase-field variable ϕ_i can be given by [15]

$$\dot{\phi}_i = -\sum_{j \neq i}^{N} \frac{2M_{ij}^{\phi}}{N} \left[\frac{\delta\Psi}{\delta\phi_i} - \frac{\delta\Psi}{\delta\phi_j} \right], \tag{4}$$

where M_{ij}^{ϕ} denotes the phase-field mobility. By taking the functional derivative of each term in Ψ in Equation (2) with respect to ϕ_i, the resulting expressions for $\delta\Psi/\delta\phi_i$ can be reformulated as

$$\frac{\delta\Psi}{\delta\phi_i} = \sum_{k=1}^{N} \left[W_{ik}\phi_k + \frac{a_{ik}^2}{2} \nabla^2\phi_k \right] + \frac{\partial\psi^b}{\partial\phi_i}. \tag{5}$$

By considering Equations (4) and (5), the difference in the partial derivatives of ψ^b with respect to ϕ_i and ϕ_j can be reformulated in terms of the driving force (ΔE_{ij}) between grains i and j as [10]

$$\frac{\partial\psi^b}{\partial\phi_i} - \frac{\partial\psi^b}{\partial\phi_j} = -\frac{8}{\pi}\sqrt{\phi_i\phi_j}\Delta E_{ij}. \tag{6}$$

After calculating the functional derivatives, the evolution equation of the phase field can be obtained as [10]

$$\dot{\phi}_i = -\sum_{j \neq i}^{N} \frac{2M_{ij}^{\phi}}{N} \left[\sum_{k=1}^{N} \left[\left[W_{ik} - W_{jk}\right]\phi_k + \frac{1}{2}\left[a_{ik}^2 - a_{jk}^2\right]\nabla^2\phi_k \right] - \frac{8}{\pi}\sqrt{\phi_i\phi_j}\Delta E_{ij} \right], \tag{7}$$

where a_{ij}, W_{ij}, and M_{ij}^{ϕ} are defined in terms of the grain boundary thickness η, grain boundary energy γ_{ij}, and grain boundary mobility M_{ij} as [10]

$$a_{ij} = \frac{2}{\pi}\sqrt{2\eta\gamma_{ij}}, \tag{8}$$

$$W_{ij} = \frac{4\gamma_{ij}}{\eta}, \tag{9}$$

$$M_{ij}^{\phi} = \frac{\pi^2}{8\eta} M_{ij}. \tag{10}$$

For simplicity, it is assumed that all grain boundaries are high-angle boundaries, with uniform grain boundary energy $\gamma_{ij} = \gamma$ and mobility $M_{ij} = M$. Consequently, the grain boundary mobility M can be expressed as [10]

$$M = \frac{M_0}{T} \exp\left[\frac{-Q_b}{RT}\right], \tag{11}$$

where M_0 is a constant, Q_b is the activation energy for grain boundary migration, R is the universal gas constant, and T is the absolute temperature.

2.2 | Dislocation Evolution Model

Dislocation dynamics predominantly govern the evolution of stored energy within the material. Under the application of strain, dislocations tend to accumulate and subsequently annihilate, thereby altering the internal microstructure of the material. The driving force term (ΔE_{ij}) in Equation (7) can be reformulated in terms of the difference in dislocation densities as [16]

$$\Delta E_{ij} = \frac{1}{2}\mu b^2\left[\rho_i - \rho_j\right], \tag{12}$$

where μ is the shear modulus, b is the Burgers vector, and ρ_i and ρ_j represent the dislocation densities in the adjacent grains i and j, respectively. The variation of dislocation density (ρ) with strain (ϵ) can be effectively described using the Kocks–Mecking (KM) model [17], which is expressed as

$$\frac{d\rho}{d\epsilon} = k_h\sqrt{\rho} - k_r\rho, \tag{13}$$

where k_h denotes the work hardening constant, while k_r represents the dynamic recovery coefficient, which depends on both the temperature T and the strain rate $\dot{\epsilon}$ [10]. The correlation between k_r and k_h can be formulated using the steady-state stress σ_{st}, and the dislocation interaction coefficient α, and is given according to [10] by

$$k_r = \frac{\alpha\mu b k_h}{\sigma_{st}}. \tag{14}$$

Following [10], the steady-state stress σ_{st} can be expressed as a function of the empirical constants A_1 and A_2, the activation energy for deformation Q_a, and the strain rate $\dot{\epsilon}$ as

$$\sigma_{st} = \left[A_1\dot{\epsilon}\left[\exp\frac{Q_a}{RT}\right]\right]^{\frac{1}{A_2}}. \tag{15}$$

The macroscopic stress is formulated as

$$\sigma = \alpha\mu b\sqrt{\bar{\rho}}, \tag{16}$$

where $\alpha = 0.5$ and $\bar{\rho}$ is the average dislocation density. Therefore, the mechanical equilibrium is not exactly solved, where the stress is obtained via solving Equations (13) and (16).

2.3 | Nucleation Criteria

During DDRX, the nucleation rate per unit area of the grain boundary $\dot{J}$, can be expressed as [16]

$$\dot{J} = C\dot{\epsilon}^m \exp\left[\frac{-Q_a}{RT}\right]. \tag{17}$$

In this context, C and m represent constants that are specific to the material. Nucleation is treated as a spontaneous process at grain boundary lattice points where the local dislocation density exceeds the critical threshold ρ_c. The total number of grain boundary lattice points satisfying this condition is denoted by n_{gb}. To ensure consistency with the macroscopic nucleation rate $\dot{J}$, a nucleus is selected at every Δn of these points, where Δn is defined according to [16]

$$\Delta n = \frac{\eta}{\dot{J}\,\Delta t\,n_{gb}\,[\Delta x]^2}, \tag{18}$$

where Δt represents the time increment and Δx is the grid spacing. The critical dislocation density ρ_c can be formulated as

$$\rho_c = \left[\frac{\sigma_c}{\alpha\mu b}\right]^2. \tag{19}$$

3 | Numerical Implementation

The phase-field model for DDRX, implemented using a finite difference scheme, is shown in Figure 1. The simulation begins with the initialization of a polycrystalline microstructure, which is generated using a grain growth model. In this stage, randomly distributed nuclei are introduced and allowed to grow, resulting in an initial microstructure described by Equation (7). To simplify the formulation, a constant driving force is applied in the phase-field equation for the term ΔE_{ij}, instead of using the dislocation density difference as described in Equation (12). Once the initial microstructure is established, a uniform initial dislocation density, ρ_{ini}, is assigned throughout the simulation domain. The DDRX process is then simulated by evolving both the dislocation density and the grain structure based on the predefined nucleation criteria, continuing until the target strain is reached. The model parameters used in this study are primarily based on previous works, particularly [10] and [16].

Simulations are performed at a constant temperature $T = 800$ K with a time step of $\Delta t = 0.01$ s. The DDRX model starts with 17 initial grains in a domain of size $N_x = 512$, $N_y = 444$, using a grid spacing of $\Delta x = 5$ μm. Grain boundary energy is $\gamma_{ij} = 0.208$ Jm^{-2}, and boundary thickness is $\eta = 4\Delta x$. M is computed with $M_0 = 0.2$ m^{4}KJ^{-1}s^{-1} and activation energy $Q_b = 92$ kJmol^{-1}. In the KM model, key parameters include: $k_h = 4\times10^8$ m^{-1}, $\mu = 30$ GPa, and $b = 2.56\times10^{-10}$ m. The steady-state stress σ_{st} is evaluated with $A_1 = 2\times10^{44}$, $A_2 = 7.6$, and $Q_a = 152$ kJmol^{-1}. The critical stress for nucleation is $\sigma_c = 40$ MPa. Additional parameters are: $C = 1\times10^{22}$, $m = 1$, $\rho_{\text{ini}} = 1\times10^9$ m^{-2}, and $\rho_c = 5.5098\times10^{13}$ m^{-2}. Periodic boundary conditions are applied during the simulation.

4 | Results

4.1 | Microstructure Evolution

During plastic deformation, the dislocation density evolves according to the KM model, which captures dislocation accumulation and dynamic recovery mechanisms. Once the local dislocation density exceeds the critical threshold ρ_c, the material attains sufficiently high internal stress and stored energy to render the nucleation of new grains energetically favorable. At this juncture, new grains are nucleated at existing grain boundaries and are initialized with a dislocation density of ρ_{ini}, as shown in Figure 2a–f. This process marks the onset of DDRX, which reshapes the microstructure by generating equiaxed grains with necklace shape microstructure.

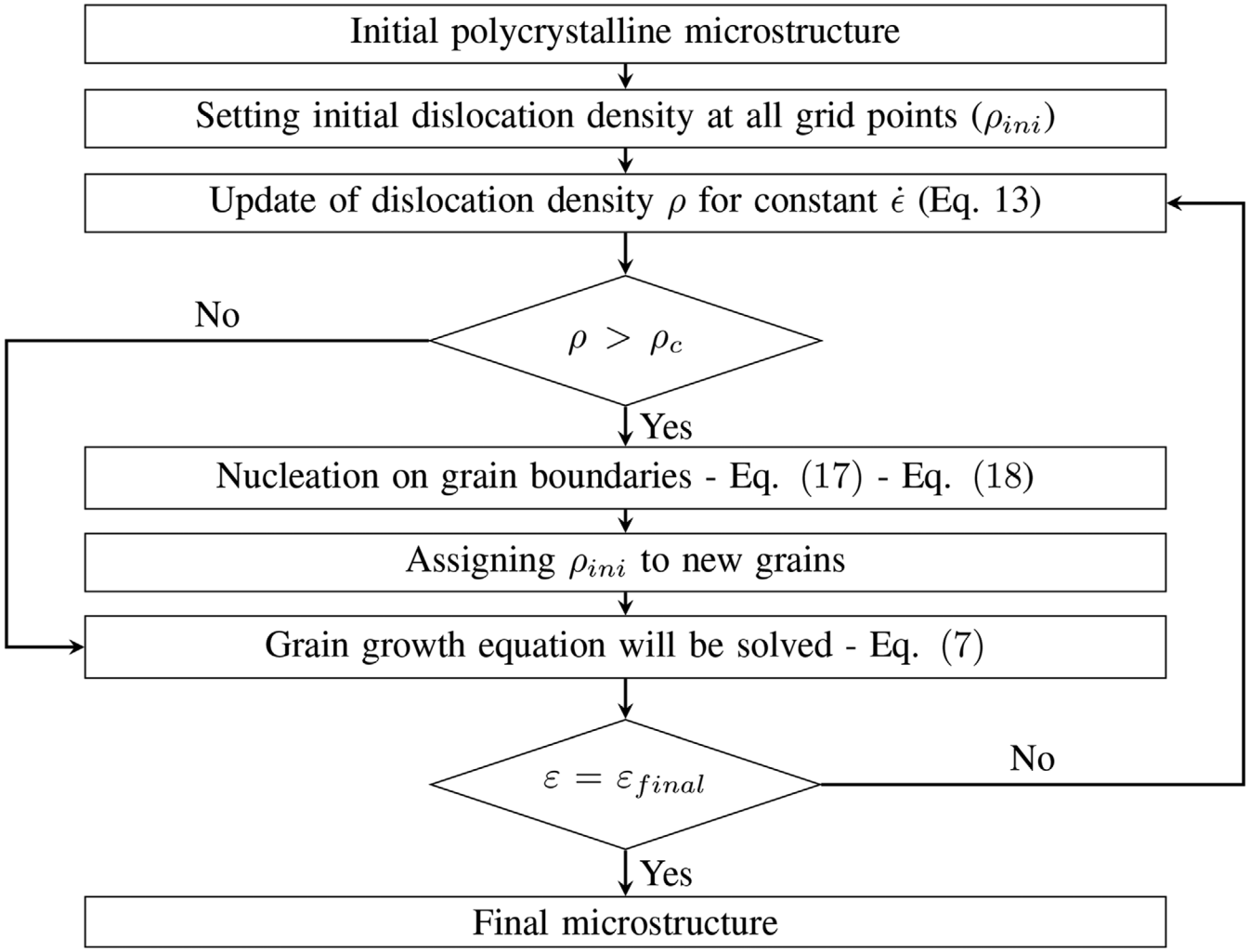

FIGURE 1 | Flowchart illustrating the sequence of calculations performed to obtain the DDRX microstructure in the model. The final microstructure is achieved once the true strain ϵ reaches its target value(ϵ_{final}), which is set to 50% across all simulations. DDRX, discontinious dynamic recrystallization.

As illustrated in Figure 2g, the average grain diameter undergoes significant refinement, decreasing from 67.25 μm initially to 11.29 μm at $t = 11$ s, and reaching a minimum of 8.07 μm at $t = 26$ s. The steep decline from 67.25 to 21.26 μm and subsequently to 8.94 μm reflects the rapid grain refinement characteristic of DDRX initiation, driven by localized dynamic softening and nucleation of new grains. Following the initial refinement, grain sizes show non-monotonic fluctuations between 11.29 and 8.94 μm, reflecting the cyclic nature of DDRX, where strain-induced boundary migration promotes growth while new grains form. By $t = 50$ s, the grain size stabilizes around 8.94 μm, indicating a dynamic equilibrium between growth and nucleation.

4.2 | Stress–Strain Behavior

The stress–strain response was analyzed at various strain rates, focusing on how microstructure characteristics affect the material behavior, as shown in Figure 3. At all strain rates, the curves in Figure 3e show distinct peak stresses followed by softening of DDRX due to nucleation and growth of strain-free grains that reduce dislocation density. At low strain rates (e.g., $\dot{\epsilon} = 0.005\ s^{-1}$), softening is gradual and stable, allowing sufficient time for grain growth and microstructure homogenization. As strain rate increases, peak stress rises, and the stress–strain curves exhibit oscillations and stress drops, especially at $\dot{\epsilon} = 0.1\ s^{-1}$, indicating repeated DDRX cycles. Under high strain rates, work hardening is so rapid that stresses climb to a higher maximum before DDRX softening sets in. Beyond 40% strain, all curves reach a steady state, indicating dynamic equilibrium where dislocation generation is balanced by annihilation and recovery, stabilizing microstructure and mechanical properties.

From the microstructural viewpoint shown in Figure 3a–d and the average grain diameters shown in Figure 3f, the grain size decreases progressively with increasing strain rate. At a strain rate of $\dot{\epsilon} = 0.005\ s^{-1}$, the average grain diameter is 9.85 μm, which decreases to 6.33 μm at $\dot{\epsilon} = 0.1\ s^{-1}$. At low strain rates, coarse grains are formed, leading to dynamic softening and lower steady-state stress. At intermediate strain rates, moderate grain sizes are produced, balancing hardening and softening. At high strain rates, DDRX leads to the formation of fine grains and higher true stresses. Therefore, strain rate plays a pivotal role in governing microstructure evolution during solid-state processing.

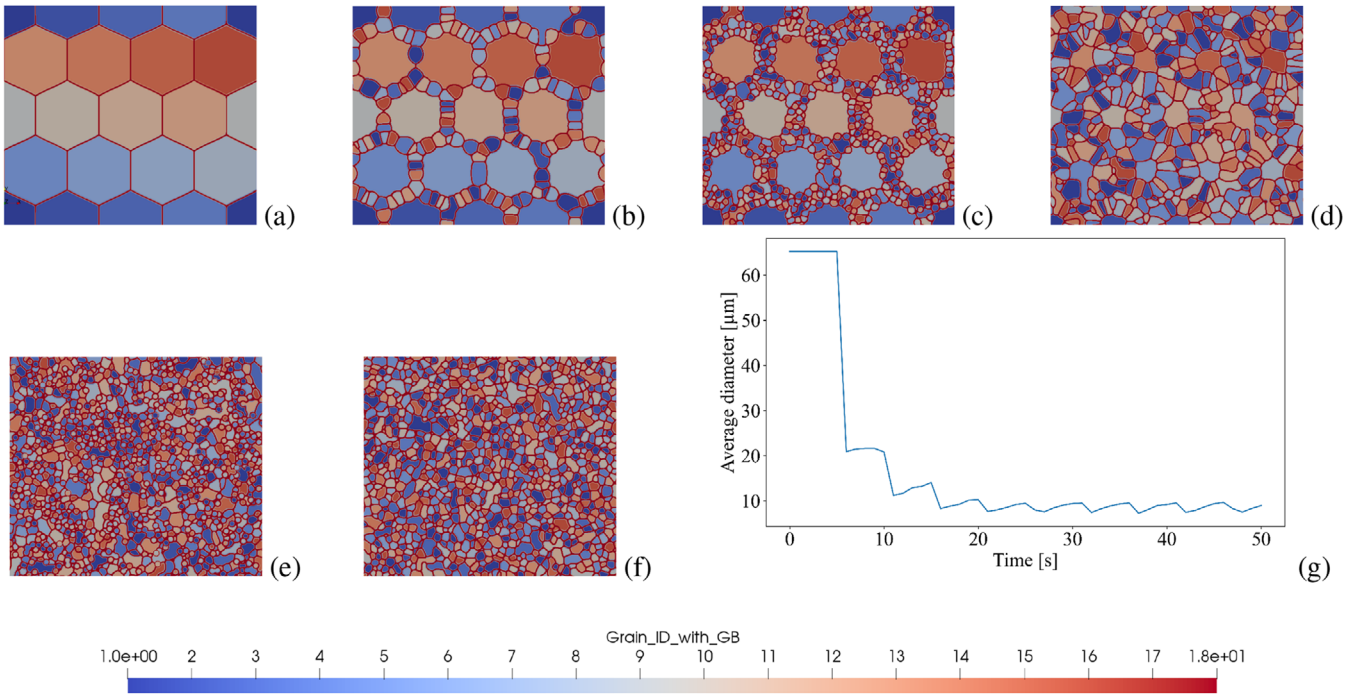

FIGURE 2 | Microstructure evolution during DDRX at selected time intervals under a constant strain rate of $\dot{\varepsilon} = 0.01\ s^{-1}$: (a) $t = 0$ s, (b) $t = 10$ s, (c) $t = 11$ s, (d) $t = 15$ s, (e) $t = 26$ s, and (f) $t = 50$ s. (g) Corresponding average grain diameter for each microstructure. The color map distinguishes individual grain IDs, each representing a unique crystallographic orientation.

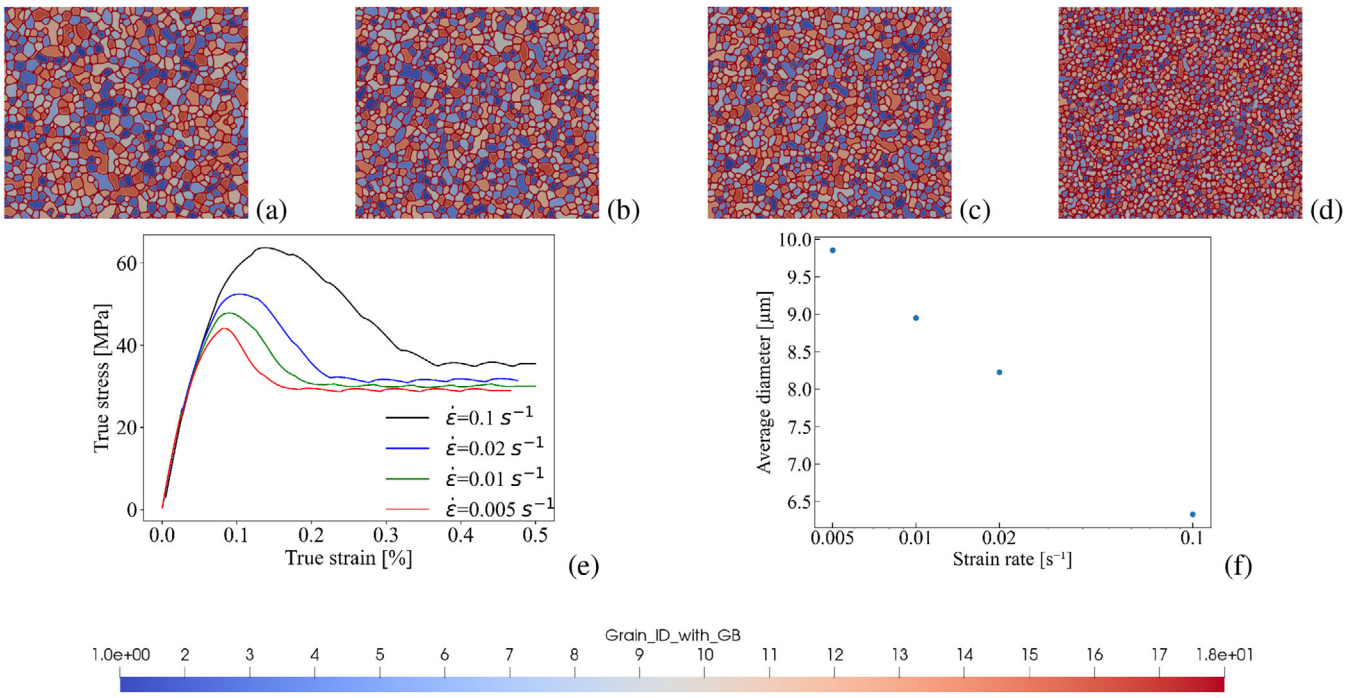

FIGURE 3 | Microstructure evolution during deformation at various strain rates at 50% deformation: (a) $\dot{\varepsilon} = 0.005\ s^{-1}$ at $t = 100$ s, (b) $\dot{\varepsilon} = 0.01\ s^{-1}$ at at $t = 50$ s, (c) $\dot{\varepsilon} = 0.02\ s^{-1}$ at $t = 25$ s, and (d) $\dot{\varepsilon} = 0.1\ s^{-1}$ at $t = 5$ s. (e) Corresponding stress–strain curves for the strain rates presented above. (f) Distribution of average grain sizes corresponding to each applied strain rate. The color-map represents grain IDs associated with different crystallographic orientations.

The onset of DDRX is largely determined by the progressive build-up of dislocations throughout deformation. At elevated strain rates, dislocations accumulate rapidly, increasing the stored energy and enhancing the driving force for DDRX. This promotes more extensive recrystallization, leading to the formation of a fine grain microstructure. The refined grains act as effective barriers to dislocation motion, hindering further dislocation movement and systematically showing higher true stresses at elevated strain rates. In the present framework, the interplay between microstructure evolution and hardening is captured through the dislocation density. At higher strain rates, the KM law predicts larger ρ because dynamic recovery is reduced, which raises the macroscopic stress via $\sigma \propto \sqrt{\rho}$. Concurrently, an increased ρ promotes grain-boundary nucleation when $\rho > \rho_c$, leading to grain refinement and associated softening. The steady-state stresses reflect a dynamic balance between strain hardening and softening.

5 | Conclusion

An MPF model was successfully used to study microstructure evolution during DDRX. As dislocation density exceeds a critical threshold, new strain-free grains nucleate at boundaries, rapidly refining the microstructure. Strain rate plays a critical role in microstructure evolution and mechanical response. At lower strain rates, extended deformation time promotes grain growth and progressive softening. In contrast, higher strain rates enhance dislocation accumulation, resulting in grain refinement and elevated true stresses. Over time, a dynamic balance between dislocation generation, recovery, and recrystallization is established, stabilizing both grain size and macroscopic stress and emphasizing the close relationship between microstructure and mechanical behavior.

Acknowledgments

This project has received funding from the European Research Council (ERC) under the European Union's Horizon 2020 research and innovation programme (grant agreement No 101001567).

Open access funding enabled and organized by Projekt DEAL.

Data Availability Statement

The data related to this research are available online https://doi.org/10.5281/zenodo.15738792.

References

1. W. Miller, L. Zhuang, J. Bottema, et al., "Recent Development in Aluminium Alloys for the Automotive Industry," *Materials Science and Engineering: A* 280 (2000): 37–49.

2. A. R. Safi, E. Mathew, R. Chafle, and B. Klusemann, "A Multi-Component Phase-Field Model for T1 Precipitates in Al-Cu-Li Alloys," *Modelling and Simulation in Materials Science and Engineering* 33, no. 6, 2025 065009.

3. U. Suhuddin, S. Mironov, H. Krohn, M. Beyer, and J. F. D. Santos, "Microstructural Evolution During Friction Surfacing of Dissimilar Aluminum Alloys," *Metallurgical and Materials Transactions A* 43 (2012): 5224–5231.

4. U. F. Suhuddin, L. Rath, R. M. Halak, and B. Klusemann, "Microstructure Evolution and Texture Development During Production of Homogeneous Fine-Grained Aluminum Wire by Friction Extrusion," *Materials Characterization* 205 (2023): 113252.

5. R. M. Halak, L. Rath, U. F. H. R. Suhuddin, J. F. dos Santos, and B. Klusemann, "Changes in Processing Characteristics and Microstructural Evolution During Friction Extrusion of Aluminum," *International Journal of Material Forming* 15, no. 3 (2022): 24.

6. J. Gandra, H. Krohn, R. Miranda, P. Vilaça, L. Quintino, and J. dos Santos, "Friction surfacing—A Review," *Journal of Materials Processing Technology* 214, no. 5 (2014): 1062–1093.

7. K. Huang and R. E. Logé, "A Review of Dynamic Recrystallization Phenomena in Metallic Materials," *Materials & Design* 111 (2016): 548–574.

8. R. Goetz and V. Seetharaman, "Modeling Dynamic Recrystallization Using Cellular Automata," *Scripta Materialia* 38 (1998): 405–413.

9. P. Peczak, "A Monte Carlo Study of Influence of Deformation Temperature on Dynamic Recrystallization," *Acta Metallurgica et Materialia* 43 (1995): 1279–1291.

10. T. Takaki, T. Hirouchi, Y. Hisakuni, A. Yamanaka, and Y. Tomita, "Multi-Phase-Field Model to Simulate Microstructure Evolutions During Dynamic Recrystallization," *Materials Transactions* 49 (2008): 2559–2565.

11. Y. Li, S. Hu, E. Barker, N. Overman, S. Whalen, and S. Mathaudhu, "Effect of Grain Structure and Strain Rate on Dynamic Recrystallization and Deformation Behavior: A Phase Field-Crystal Plasticity Model," *Computational Materials Science* 180 (2020): 109707.

12. N. Moelans, B. Blanpain, and P. Wollants, "An Introduction to Phase-Field Modeling of Microstructure Evolution," *Calphad* 32 (2008): 268–294.

13. T. Takaki and Y. Tomita, "Static Recrystallization Simulations Starting From Predicted Deformation Microstructure by Coupling Multi-Phase-Field Method and Finite Element Method Based on Crystal Plasticity," *International Journal of Mechanical Sciences* 52, no. 2 (2010): 320–328.

14. I. Steinbach and F. Pezzolla, "A Generalized Field Method for Multiphase Transformations Using Interface Fields," *Physica D: Nonlinear Phenomena* 134 (1999): 385–393.

15. I. Steinbach, "Phase-Field Models in Materials Science," *Modelling and Simulation in Materials Science and Engineering* 17 (2009): 073001.

16. P. Pirhayati and H. Jamshidi Aval, "Phase-Field Microstructure Simulation During Aluminum Alloy Friction Surfacing," *Surface and Coatings Technology* 402 (2020): 126496.

17. H. Mecking and U. Kocks, "Kinetics of Flow and strain-Hardening," *Acta Metallurgica* 29 (1981): 1865–1875.